

Real-space Green's function approach for x-ray spectra at finite temperature

Tun S. Tan,* J. J. Kas, and J. J. Rehr

Dept. of Physics, Univ. of Washington, Seattle, WA 98195-1560

(Dated: March 16, 2021)

There has been considerable interest in properties of condensed matter at finite temperature, including non-equilibrium behavior and extreme conditions up to the warm dense matter regime. Such behavior is encountered, e.g., in experimental time-resolved x-ray absorption spectroscopy (XAS) in the presence of intense laser fields. In an effort to simulate such behavior, we present an approach for calculations of finite-temperature x-ray absorption spectra in arbitrary materials, using a generalization of the real-space Green's function formalism. The method is incorporated as an option in the core-level x-ray spectroscopy code FEFF10. To illustrate the approach, we present calculations for several materials together with comparisons to experiment and with other methods.

I. INTRODUCTION

X-ray absorption spectroscopy (XAS) has become an important tool for studies of materials in fields ranging from materials science and chemistry to geophysics and astrophysics [1–6]. XAS is used extensively to probe both local electronic and structural properties simultaneously at synchrotron facilities worldwide. With the development of x-ray free electron lasers (XFELs), XAS experiments have been extended to treat ultra-short femto- to picosecond time-scales and non-equilibrium conditions, with temperatures T up to many thousands of K. These capabilities are important, e.g., for studies of matter in extreme conditions as well as non-equilibrium and dynamic response due to electron-phonon energy transfer, spin-relaxation and reactions, as well as in shocked matter. The extreme conditions include the warm dense matter (WDM) regime, where $T \sim T_F$ (the Fermi temperature) and the density is within an order of magnitude or so of normal conditions,

Modern theories of optical and x-ray spectra start from the many-body Fermi's golden rule and are usually cast at zero temperature. In order to make the calculations computationally tractable, a single-particle or quasi-particle approximation for the photoelectron is often used [7, 8]. The quasi-particle approximation is the basis of the real-space Green's function (RSGF) approach used in the FEFF codes [9], which are applicable to systems throughout the periodic table. Our main aim in this work is to extend the RSGF approach for XAS to finite temperature (FT). Secondly we aim to explore FT and non-equilibrium behavior in a few systems that can be measured experimentally. Our FT generalization of the RSGF approach requires a number of extensions, since many electronic ingredients, e.g., the chemical potential, exchange-correlation potential, quasi-particle self-energy, and mean-free path are temperature dependent. Vibrational effects are also temperature dependent and strongly damp the fine-structure in XAS at high T . At low temperatures compared to

the Fermi temperature $T \ll T_F$ (which is typically a few $\times 10^4$ K), the exchange-correlation potential and self-energy are weakly temperature dependent and a zero-temperature approximation is often adequate for electronic structure. Vibrational effects become substantial when T is of order the Debye temperature T_D (which is typically a few $\times 10^2$ K). However, in the WDM regime where $T \sim T_F$, an explicit account of temperature dependence becomes necessary, since the exchange-correlation potential varies from exchange- to correlation-dominated behavior with increasing temperature in that regime [10]. At finite-temperature an efficient approximation for the XAS cross-section can be obtained using the RSGF formalism, which is the real-space analog of the KKR band structure approach [11]. As at $T = 0$, the approach is based on the one-particle electron Green's function, which is calculated either by matrix inversion or by a well converged multiple-scattering path expansion. Our current implementation builds upon the theory and algorithms used in the FEFF9 code [9], and has been incorporated in a new version FEFF10 [12]. This theory is illustrated here with a number of examples. While the theory is generally applicable to periodic or aperiodic systems alike throughout the periodic table, we focus on applications at normal densities, where the theory can be tested against recent experiment.

The remainder of the paper is organized as follows: in Sec. II. we review the quasiparticle XAS theory and present the RSGF formalism. Sec. III. treats finite temperature effects and Sec. IV. presents a number of examples. Finally Sec. V. contains a brief summary and conclusions.

II. FINITE TEMPERATURE XAS

In this section, we briefly summarize the generalization of quasiparticle theory of XAS to finite temperature. Theories of the XAS cross section typically start from the many-body Fermi golden rule

$$\sigma(\omega) = 4\pi^2 \frac{\omega}{c} \sum_F |\langle I | \hat{D} | F \rangle|^2 \delta(\omega + E_I - E_F), \quad (1)$$

* tunsheng@uw.edu

where $|I\rangle$ is the many-body ground state of the system with total energy E_I , $|F\rangle$ ranges over the many-body final states with energy E_F , and \hat{D} is the many-body transition operator due to the x-ray field, which here is taken to be a dipole-interaction $D = \sum_{i,f} d_{ij} \hat{c}_f^\dagger \hat{c}_i$ where d_{ij} are the dipole matrix elements, and c_i and c_i^\dagger are electron annihilation and creation operators respectively. Here and throughout this paper we use atomic units $e = \hbar = m = 1$, and units of temperature where $k_B = 1$, unless noted otherwise. In order to reduce the calculation to a quasi-particle framework, we make a sudden approximation as in the Δ SCF approximation, with the final-state rule [13]. Since a core electron leaves behind a hole after being excited into the photo-electron state the final photo-electron state $|\phi_f\rangle$ must take into account the interaction with the core hole potential, while a given core-level $|\phi_i\rangle$ is calculated with the initial state configuration. Next the many-particle initial and final states are factored such that $|I\rangle = |\phi_i\rangle |\tilde{\Phi}_0^{N-1}\rangle$ and $|F\rangle = |\phi_f\rangle |\tilde{\Phi}_n^{N-1}\rangle$, where $|\tilde{\Phi}_n^{N-1}\rangle$ is the n^{th} excited state of the $N-1$ electron system with a core-hole in level i , and $|\phi_f\rangle$ is the photo-electron state calculated in the presence of the core-hole. If one ignores the energy dependence of excitations of the $N-1$ electron system, Eq. (1) yields an effective single- or quasi-particle cross section $\sigma_1(\omega)$ contribution from a given core level i given by

$$\sigma_1(\omega) = 4\pi^2 \frac{\omega}{c} \sum_f |\langle i|\hat{d}|f\rangle|^2 \delta_\Gamma(\omega + \epsilon_i - \epsilon_f), \quad (2)$$

where ϵ_i and ϵ_f are the eigenenergies of the quasiparticle initial $|i\rangle$ (deep-core) and final $|f\rangle$ (photo-excited) states, and $\delta_\Gamma(\omega)$ denotes a Lorentzian of width Γ , where Γ includes the lifetime and final-state broadening. More generally this approximation can be corrected by a convolution of the quasi-particle XAS with the core spectral function, defined as $A_c(\omega) = \sum_n S_n^2 \delta(\omega - \omega_n)$ where $S_n^2 = |\langle \tilde{\Phi}_0^{N-1} | \tilde{\Phi}_n^{N-1} \rangle|^2$ is the many-body amplitude overlap integral between initial and final states. This convolution modifies the cross-section by an additional, energy dependent broadening factor [14], of unit weight which damps the fine structure by an constant factor, which historically has been denoted by S_0^2 [15].

A. Real-space Green's function

Formally the retarded single electron Green's function $G^R(\epsilon)$ in a basis of local site, angular momentum states[15] $|L, j\rangle = j_L(\mathbf{r}) Y_L(\hat{r})$ is given by the spectral sum

$$\begin{aligned} G_{L'j',Lj}(\epsilon) &= \langle L'j'|G^R(\epsilon)|L,j\rangle \\ &= \sum_f \frac{\langle L'j'|f\rangle \langle f|Lj\rangle}{\epsilon - \epsilon_f + i\delta}, \end{aligned} \quad (3)$$

where ϵ_f is the eigenenergy of the final state SCF quasi-particle Hamiltonian $H' = p^2/2 + v_f + \Sigma(\epsilon; T)$, v_f is

the effective one electron Coulomb potential in the presence of a screened core hole, and $\Sigma(\epsilon)$ is the dynamically screened FT electron self-energy. A significant advantage of the RSGF formalism is that it implicitly builds in the summation over final states f , which is a computational bottleneck in wave-function approaches at high energies [9]. In FEFF the RSGF approach implicitly includes Dirac-relativistic effects, and the angular momentum index L denotes the relativistic angular quantum numbers $L = (\kappa, m)$ [15]. In the following temperature dependence will be assumed implicitly, unless otherwise specified. By inserting the spectral representation of $G^R(\epsilon)$ into Eq. (2) together with Fermi-Dirac occupation numbers, the final states are implicitly summed in the calculation of $\sigma_{qp}(\omega)$ using the solution to the Dyson equation [16], as summarized below. Thus

$$\sigma_{qp}(\omega) = L_\Gamma(\omega) * \sigma_1^0(\omega), \quad (4)$$

where $L_\Gamma(\omega)$ is a Lorentzian function that accounts for the core-hole lifetime broadening and σ_1^0 is the single- or quasiparticle cross-section with no core-hole broadening, given by

$$\begin{aligned} \sigma_{qp}^0(\omega) &= -4\pi \frac{\omega}{c} \text{Im} \sum_{i|l'} \langle i|\hat{d}|l'\rangle G_{l'0}^R(\omega + \epsilon_i) \hat{d}^\dagger |i\rangle \\ &\quad \times f_T(\epsilon_i) [1 - f_T(\omega + \epsilon_i)], \end{aligned} \quad (5)$$

where site 0 is taken to be the absorbing atom, $f_T = 1/[\exp(\epsilon - \mu(T)) + 1]$ is the Fermi-Dirac distribution, and $\mu(T)$ is the chemical potential of the system. Much of the electronic temperature dependence is due to that in the occupation numbers f_T .

Multiple-scattering of the photoelectron by its environment is naturally built into the RSGF formalism[16]. The intra-atomic contributions from the absorbing atom G_c can be separated from the scattering atoms G_{sc} into $G^R = G_c^R + G_{sc}^R$. (For simplicity, here and below we drop the subscripts on matrix elements of G .) The scattering contribution G_{sc}^R is determined by the free Green's function G_0^R , the total scattering matrix T , and partial-wave phase shifts δ for the photoelectron state of a given angular momentum (suppressed) using the matrix inverse solution to the Dyson equation [13].

$$G_{sc}^R = e^{i\delta} (1 - G_0^R T)^{-1} G_0^R e^{i\delta'}. \quad (6)$$

For EXAFS energies (typically above about 50 eV beyond an absorption edge), the matrix inverse can be expanded in a rapidly converging series of scattering paths typically with less than 4 legs. However, for XANES, full multiple scattering (FMS) is usually needed, and can be carried out by a fast matrix inversion algorithm since the basis of relevant angular-momentum, site scattering states is small due to the short mean free path and $l_{max} < 4$.

III. FINITE-TEMPERATURE EFFECTS

Several effects come into play in the theory of XAS at finite temperatures. First, there are effects of electronic

temperature in the initial many-body electronic configuration of the system due to the temperature dependence of the electron density and chemical potential. Second, the Fermi function cutoff that defines the x-ray “edge” of the cross-section as in Eq. (5) broadens with increasing T . Third there are FT effects on the exchange and correlation, both through the exchange-correlation potential v_{xc} and the quasi-particle self-energy $\Sigma(\epsilon)$. Finally, there are the FT effects of lattice vibrations which give rise to Debye-Waller factors that strongly damp the XAS fine-structure. These effects are summarized below:

1) FT SCF: As for the ground state, in order to construct the (scattering) potential v , we implement a generalization of the self-consistent field (SCF) method to calculate the Coulomb potentials, electron densities and a temperature dependent chemical potential. In the RSGF approach in FEFF, the SCF procedure starts with the overlapped atomic electron densities obtained by solving the relativistic Dirac-Fock equations for each atom in the system. From this initial guess of the electron density, a Green’s function is calculated, which provides a new density and chemical potential. This procedure is then repeated until self-consistency ($\rho_i = \rho_{i-1}$) is reached to high accuracy, typically in about 20 iterations or so. Assuming a frozen core, the valence electron contribution to density of electrons is given in terms of an integral over energy of the imaginary part of the Green’s function,

$$\rho(r) = -\frac{2}{\pi} \int_{E_B}^{\infty} dE \operatorname{Im} G(r, r, E) f_T(E), \quad (7)$$

where E_B is the core-valence separation energy (typically set to -40 eV in FEFF), and the factor of 2 accounts for spin-degeneracy. For computational efficiency at both zero and finite temperatures, the above integral is carried out in the complex plane where the Green’s function becomes smooth. However, there is an added complication due to the possible presence of the Matsubara poles in the Fermi function. In order to include them, we integrate along a contour C (shown in Fig. 1), where the first leg traverses from E_B to $E_B + 2\pi i n k T$, then to $\infty + 2\pi i n k T$, where $2\pi i n k T$ is halfway between the Matsubara poles. For a given chemical potential, the valence density is then given by

$$\rho(r) = -\frac{2}{\pi} \operatorname{Im} \left[\int_C dE G(r, r, E) f_T(E), \right. \\ \left. -2\pi i k T \sum_{j=1}^n G(r, r, z_j) \right], \quad (8)$$

where $z_j = \mu \pm i\pi(2j-1)kT$ are the Matsubara poles, and n is the number of poles between the contour C and the real axis. Eq. (8) also has implicit dependence on the chemical potential through the Fermi function. In turn the chemical potential is found by enforcing charge neutrality,

$$N_{el} = \int dr \rho(r; \mu(T)), \quad (9)$$

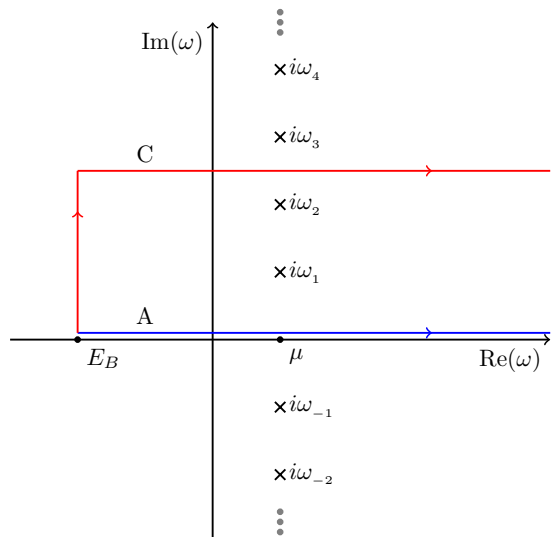


FIG. 1. Energy contour for electron density calculation at finite temperature: $\omega_j = \pi(2j-1)kT$ denotes the imaginary part of the Matsubara poles of the fermi function $f(\omega)$. The integration starts from some core-valence separation level E_B above the core states but below the valence states. Contour A (blue) represents the original integration path just above the real axis, while contour C (red) represents the integration path in the complex plane.

where N_{el} is the number of valence electrons in the system, again treating the core-electrons as frozen.

Eqs. (4) and (5) for the cross section contain similar integrals of the Green’s function multiplied by the Fermi function. These integrals are dealt with in a similar manner, although the contour is slightly different, in principal extending from $-\infty + i2\pi n k_B T$ to $+\infty + i2\pi n k_B T$. There is also an additional pole arising from the Lorentzian broadening function $L_\Gamma(\omega)$.

2) FT exchange-correlation potentials: Additional temperature dependence comes from that in the exchange-correlation potentials (which affect the initial state densities and potentials). An approach for calculating these exchange-correlation potentials from first principles with a FT cumulant Green’s function approach has been discussed by Kas et al.[10] which shows that the potentials cross-over from exchange- to correlation-dominated with increasing T . Here, the behavior is treated by an efficient parameterized extension of DFT fit to Quantum-Monte Carlo calculations (QMC) by Karasiev et al. [17], which is in good agreement with the results of Kas et al. [10].

3) FT Self-energy effects: The temperature dependence of the dynamical quasiparticle self-energy becomes important in calculations of the quasi-particle photoelectron states and hence the transition matrix elements at energies above an edge. Since full calculations of the FT self-energy[18] are computationally demanding, we have used a much more efficient FT COHSEX approximation to the GW self-energy for this purpose [19].

4) Lattice vibrations: As at $T = 0$ Lattice vibrations strongly damp electron scattering at high energy. Approximate calculations at temperatures up to several times the Debye-temperature can be done by including Debye-Waller factors $\exp(-2\sigma^2 k^2)$ in the Green's function propagator or multiple scattering paths. This can be done using the correlated Debye model and mean square radial displacements $\sigma^2(T) \propto T/T_D$, where T_D is the Debye temperature. However, this approach becomes inapplicable in the near edge regime (where symmetry breaking occurs) and at high temperatures $T \gg T_D$, where the quasi-harmonic approximation breaks down. For those cases a configurational average is called for. At temperatures well above T_D , one can use finite- T molecular dynamics (MD) to obtain a temperature dependent configurational average of the spectrum. Closer to zero temperature, zero-point motion can also be included via Quantum-Monte-Carlo sampling.

IV. CALCULATIONS

A. Simple Metal: Al

Aluminum (fcc Al) is a prototypical nearly-free-electron system for testing electronic structure calculations. The electronic density of states (DOS) for Al in the conduction band is similar to that for a free electron model, with a square root like dispersion at the bottom of the band. We show the chemical potential shift vs electron temperature T_e for aluminum up to $T_e = 10$ eV (1 eV = 11604 K) in Fig. 2. For $T = 0$ we used the von Barth Hedin (v_{xc}^{VBH}) exchange-correlation potential [20] and for $T > 0$ the temperature dependent approximation of KSDT (v_{xc}^{KSDT}) [17]. Our v_{xc}^{VBH} chemical potential agrees well with the calculations of Lin et. al [21] up to $T = 4$ eV, and is reasonably accurate up to about 10 eV, consistent with the T^2 behavior of the Sommerfeld expansion. Remarkably the Sommerfeld-expansion remains a good approximation even at very high T of order several eV.

Next, we investigate the temperature dependence of the K-edge XAS of Al at normal density up to WDM temperatures. We show the calculated K-edge XAS for electron temperatures $T_e = 0.025, 0.5,$ and 3.0 eV in Fig. 3. The behavior at the edge is consistent with broadening of the Fermi-Dirac distribution due to the nearly free electron density of states of Al. The ‘‘pre-edge’’ behavior is due to the increasing contribution from previously occupied states below the $T = 0$ Fermi level.

In order to account for thermal vibrations, we use the correlated Debye model ($T_D = 430$ K. For comparison we show DFT based XAS calculated using quantum molecular dynamics (QMC) averaged over several QMD runs [22]. Investigations of the Al K-edge under isochoric heating ($T_e = T_L$) at normal density were also done,[22] with measurements at temperatures $T_e = T_L = 0.025, 0.09, 0.27, 1.40$ and 1.76 eV, as in Fig. 4. Our calculation with

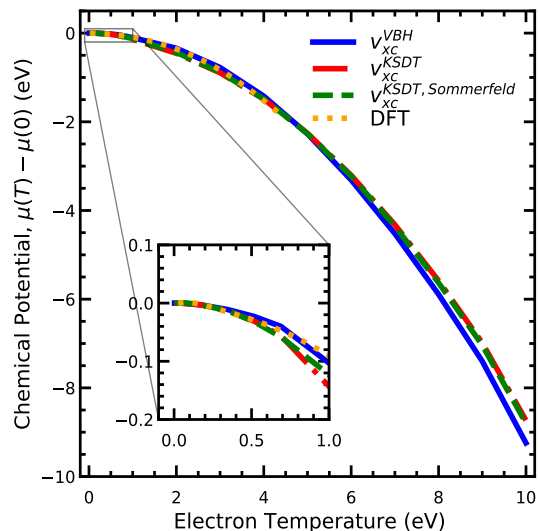


FIG. 2. Chemical potential shift for aluminum, $\mu(T) - \mu(0)$ versus electron temperature, T_e using the ground state von Barth-Hedin [20] (blue) and finite T KSDT [17] (red) exchange-correlation potentials. For comparison the $T = 0$ K DFT calculation [21] (orange) is also shown up to $T = 4$ eV. The result with the Sommerfeld expansion (green) is shown for KSDT exchange-correlation potential. The inset shows the chemical potential shift up to $T = 1$ eV.

the correlated Debye model agrees with fairly well with these results. In principle, the correlated Debye model breaks down at high temperatures ($T > 0.27$ eV) when anharmonicity becomes large, but this is not a serious problem as the fine-structure in the XAS is largely suppressed at these high temperatures.

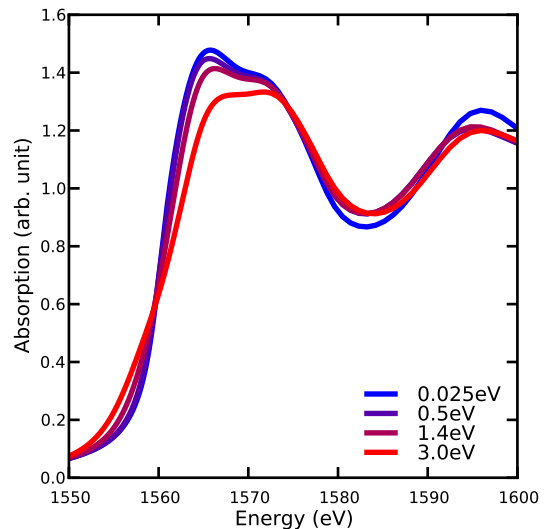


FIG. 3. K-edge XAS for aluminum vs electron temperature including only temperature dependent KSDT exchange correlation potentials (see text). Note that the edge broadens considerably with increasing temperature.

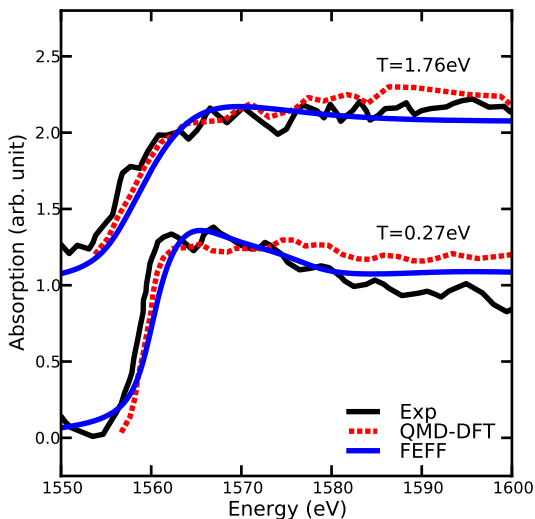


FIG. 4. Calculated K-edge XAS for equilibrium Al ($T_e = T_L$) at solid density vs experimental XAS at $T = 0.27$ and 1.76 eV. From bottom to top, QMD-DFT are simulated at $T = 0.43$, 0.86 and 0.07 eV while FEFF simulation are done at $T = 0.27$, 1.4 and 3.0 eV. Note the substantial broadening of the edge at increased T , roughly consistent with experiment, and that lattice vibration effects completely damp the fine-structure. The fluctuations in the experimental XAS reflect experimental noise.

B. Warm Dense Cu

Being a noble transition metal, Cu has substantially different excited-state properties compared to simple nearly free electron metals like aluminum, due to the highly localized d -band just below the Fermi level. Hence, at elevated temperatures, the XAS also differs. Several works [4, 23–25] studied these changes in the $L_{2,3}$ -edge of Cu XAS in WDM using a more computationally expensive AIMD simulation. Here we investigate the XAS of Cu using our SCF RSGF approach and the correlated Debye model. Fig. 5 shows the simulated XANES spectra at normal density for various temperatures. Our calculation is broadened with a Gaussian to match that in the the DFT-based calculation [26]. As expected, the pre-edge structure in the XAS can be attributed to the increasing contribution from the d -states as the Fermi-Dirac distribution broadens with increasing T [4, 23–25]. Conversely, states just above the Fermi level have a reduced contribution leading to a smaller peak just above the edge. The changes in XAS due to electronic temperature are mainly localized in the near edge, whereas that due to the lattice temperature affects the region above the edge, especially the fine structure.

The edge-shift and the pre-edge area are both candidates for assessing the internal temperature of a system. In order to extract the edge shift and pre-edge area, the edge position is defined to be the first local maximum of the first derivative in the reference XANES spectrum.

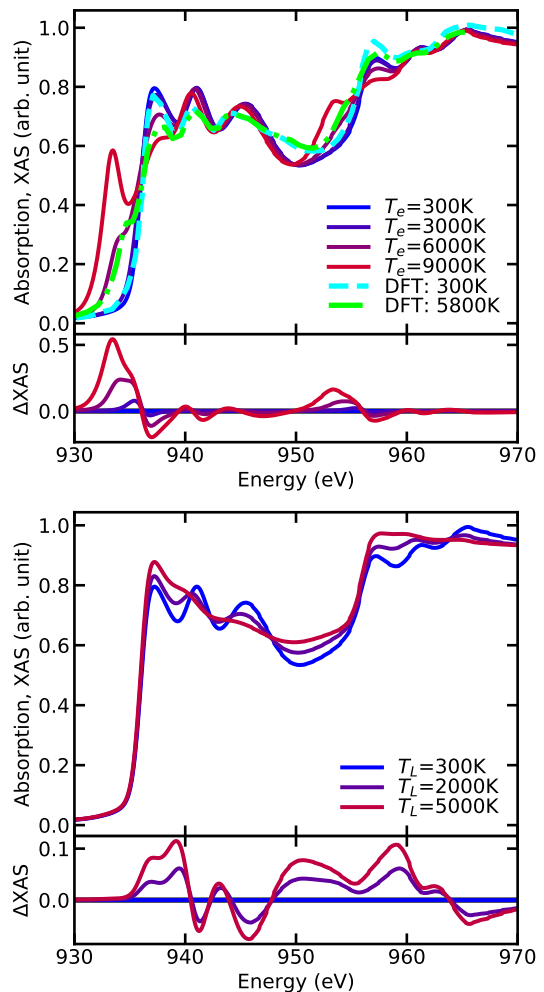


FIG. 5. L_3 -edge XAS of Cu at normal density for (Top) electron temperature $T_e = 300$ K up to 9000 K at lattice temperature $T_L = 300$ K; and (Bottom) for lattice temperature $T_L = 300$ K up to 5000 K at electron temperature $T_e = 300$ K. The DFT calculation [26] is shown for $T_e = 300$ K (light blue) and 5800 K (green). The lower panels show the change in XAS with respect to normal conditions $T_e = T_L = 300$ K.

The electron temperature dependence of the edge shift and pre-edge area are shown in Fig. 6. Note that the pre-edge area is monotonically increasing with the electron temperature and it becomes linearly correlated to T_e above 6000 K, consistent with previous results.[26] In contrast the edge-shift is highly non-linear, exhibiting an abrupt shift at about 7000 K. Therefore, for Cu and probably for other transition metals as well, the pre-edge area is a better proxy for an electron temperature thermometer, compared to the edge shift.

Next, we compare our finite-temperature calculation to time-resolved, WDM experiments [4]. The system being explored is a 70 nm copper foil heated optically by a 400 nm laser at a fluence of 0.33 J/cm². As a consequence the electrons are optically excited leading to an initial huge pre-edge peak below the L_3 -edge. In order to model

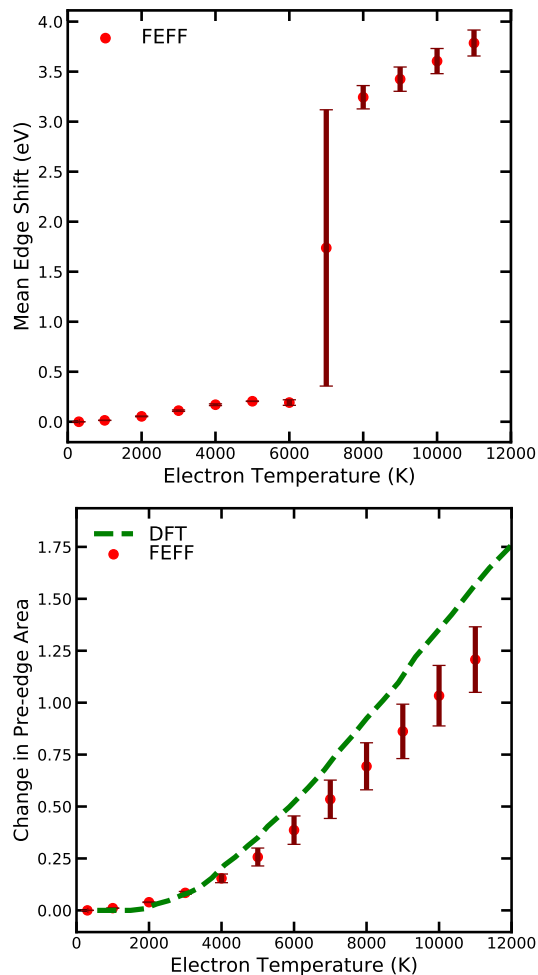


FIG. 6. (Top) Edge shift in the L_3 -edge of Cu as a function of electron temperature (red); the sudden shift is due to the onset of the d -band edge. (Bottom) Change in pre-edge area as a function of electron temperature. The DFT calculation (green dashes) [26] was computed using ABINIT at lattice temperature $T_L = 300$ K. Note that in contrast to the edge shift, the pre-edge area varies smoothly with temperature for Cu.

the temperature evolution, we used a two-temperature (2T) model.[4] with the same parameters for the electron heat capacity and electron-phonon coupling factor as in Zhibin et al. [21]. The temperature evolution is shown in Fig. 7. Note that the lattice temperature raises quickly above the melting temperature ~ 1358 K under 1 ps due to the strong electron-phonon coupling in copper. Our simulations use XAS from 20 atomic configurations taken from QMD calculations using the VASP code [27, 28] with generalized gradient approximation (GGA) exchange-correlation potentials [29]. We also used the PAW potentials with an energy-cutoff of 590 eV. The system with a $2 \times 2 \times 2$ supercell constructed from a conventional unit cell of 8 atoms is propagated with a time step of 1 fs to reach equilibration, and the sampling of configurations is performed by randomly sampling from a

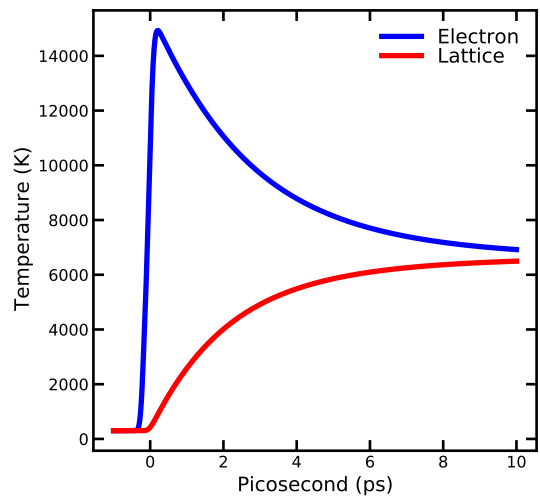


FIG. 7. Dynamics of electron temperature (blue) and lattice temperature (red) based on two-temperature model calculation. The absorption power is calculated using Beer-Lambert law for a Gaussian profile 400 nm laser source for a 70 nm thick copper.

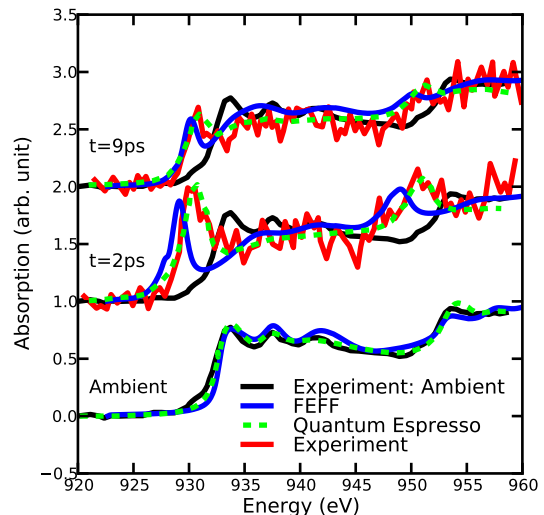


FIG. 8. Time-resolved XANES for 70 nm copper at different delay-times $t=2$ ps and 9 ps. The experimental measurement (red) is averaged over 150 snapshots. The ambient condition measurement is averaged over 70 ps. Our calculations (blue) for different times are computed at $T_e = 10200$ K and 6000 K. The DFT results[4] (green) are calculated using the Quantum Espresso code at the same temperatures.

2 ps long trajectory with a time step of 1 fs. We compare our simulation at temperatures $T_e = 300$ K, 10200 K and 6000 K for the time-delays $t < 0$ ps, $t = 2$ ps and $t = 9$ ps respectively, with those from DFT-based calculations[4] in Fig 8. Note that our calculation underestimates the Fermi level for $T_e = 10200$ K ($t = 2$ ps) by a few eV, leading to the observed shift in the XANES.

C. Transition Metals: Ti and Au

As examples of other FT L_3 -edge XAS calculations, we present FT calculations for an early transition metal (titanium), where the d -bands are partially filled, and for a late transition metal (gold) where the d -bands are full. Fig. 9. shows the temperature dependence of the L -edges of these materials. The XANES of Ti is blue-shifted with increasing temperature because the chemical potential is located in the middle of the d -band and the density of states above the chemical potential is higher. Also, the broadening of the Fermi-Dirac distribution includes a wider energy range of d -states in the transition, which affects the onset of the pre-edge. In contrast, the XANES of gold (Au) is red-shifted, as shown in bottom

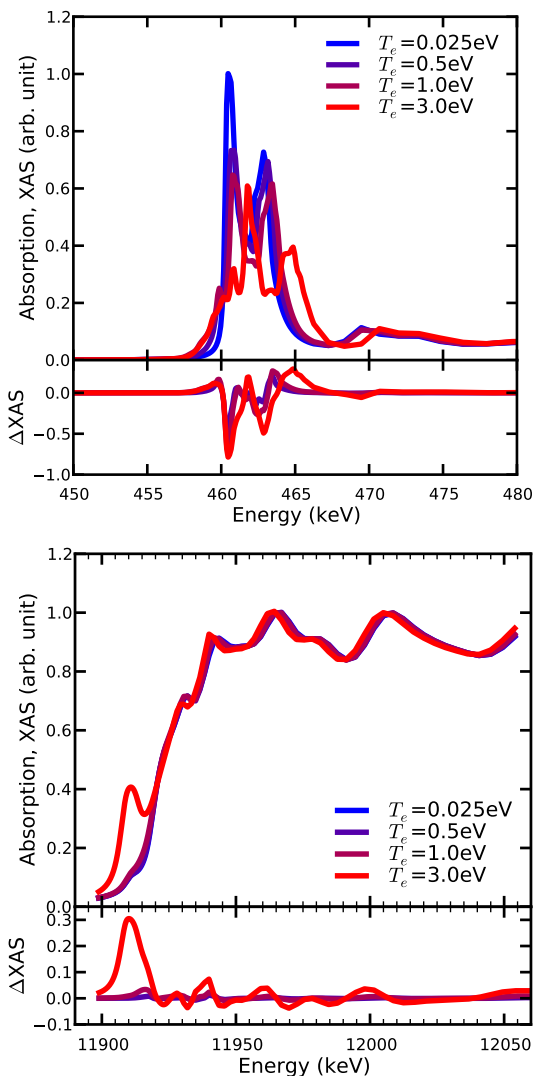


FIG. 9. L_3 -edge absorption for titanium (Top) where the structure reflects that of the unfilled d -bands, and gold (Bottom) where the d -bands are nearly filled. The difference ΔXAS between the XAS at finite T and zero temperature is also shown.

plot of Fig. 9. This opposing behavior is due to the higher density of states below the chemical potential. Again, the onset of the pre-edge structure is due to the broadening of the Fermi-Dirac distribution and shift of the chemical potential.

D. MgO

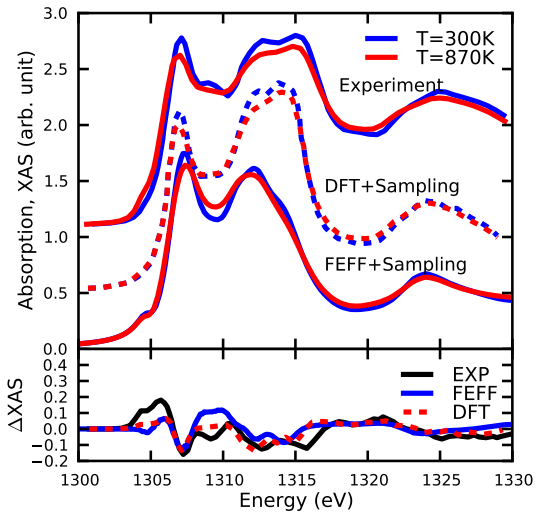


FIG. 10. Mg K-edge spectra for MgO at temperature $T=300$ K (blue) and 870 K (red). The top plot shows the experimental spectra[37], the DFT spectra [37] and the FEFF quasi-harmonic spectra. The bottom plot shows the spectra difference with respect to $T=300$ K for the experiment (solid black), FEFF (solid blue) and DFT (dashed red) are shown.

As a final example, we present results for the Mg K-edge XANES of MgO with FT lattice behavior calculated using the quasi-harmonic approximation. Fig. 10 shows the average XAS for 30 randomly sampled configurations at equilibrium temperatures $T_e = T_l = 300$ K and 870K. The configurations are obtained by sampling the normal modes calculated from dynamical matrices at the experimental lattice constants and the given temperatures using Quantum Espresso code [30–32], with GGA functional[33] for a 16-atom $2 \times 2 \times 2$ supercell constructed from a primitive cell. The electronic density of state is computed with a $6 \times 6 \times 6$ k-point grid with an energy cutoff of 58 Ry. Next, we use the density-functional perturbation theory to compute the dynamical matrix calculation at the Γ -point. The long range electric fields is accounted for from the calculation of the Born effective charge.

The FEFF calculations are found to overestimate the screening effect of light element oxides [34]. Instead of using the ad-hoc $Z + 1$ approach to overcome the strong screening effect of the final state rule, we used the random-phase approximation (RPA) for the core hole screening in FEFF. The RPA is more accurate in this

case, being similar to a Bethe-Salpeter equation. [35, 36] Finally, we add an additional energy shift of 2.6 eV to the chemical potential. As a comparison, we show the experiment and DFT calculation by Nemausat *et al.* using the stochastic self-consistent harmonic approximation[37] in Fig. 10. Our muffin-tin potential model predicts a smaller excitations between 1310 eV and 1315 eV.

V. CONCLUSIONS

We have extended the real-space Green's function theory of XAS [15] to finite temperatures (FT) up to the warm-dense matter regime $T \approx T_F$. Our FT generalization takes into account both electron temperature and lattice temperature effects. Briefly, a FT SCF procedure is carried out in the complex energy plane in terms of the FT one-electron Green's function. This builds in the FT exchange-correlation potential, using the KSDT parameterization. The FT self-energy is also important for XAS, since it accounts for final-state effects in the spectra including corrections to shifts and broadening. While dynamic exchange effects can also be included, due to the difficulty calculating the FT self-energy, a more efficient FT COHSEX approximation has been used. An important difference from the $T = 0$ theory of the XAS is an account of smearing of the Fermi level

due to FT occupation numbers. Vibrational effects are included in terms of a correlated Debye model for the fine-structure at low T in XAS or a configurational average for XANES at high T . The FT generalization introduced here is implemented as an extension of the FEFF codes in a new version FEFF10 [12]. The approach has been tested against various experiments, and typically yields good quantitative agreement. We believe these developments may be useful in interpretation of many experiments, e.g., for studies non-equilibrium behavior, extreme conditions, and shocked conditions. The approach can also be used to differentiate between lattice and electron temperature effects.

ACKNOWLEDGMENTS

We thank R. Albers, B. Fultz, D. Prendergast, G. Seidler, S. Trickey, F. Vila, and H. Wende for comments and suggestions. This work is supported by DOE BES Grant DE-FG02-97ER45623. The development of FEFF10 carried out within the Theory Institute for Materials and Energy Spectroscopies (TIMES) at SLAC, and is supported by the U.S. DOE, Office of Basic Energy Sciences, Division of Materials Sciences and Engineering, under contract DE-AC02-76SF00515.

-
- [1] A. Savin, Shelley L.P. and Berko, A. N. Blacklocks, W. Edwards, and A. V. Chadwick, *Comptes Rendus Chimie* **11**, 948 (2008).
 - [2] G. J. Sherborne and B. N. Nguyen, *Chemistry Central Journal* **9**, 37 (2015).
 - [3] F. Lin, Y. Liu, X. Yu, L. Cheng, A. Singer, O. G. Shpyrko, H. L. Xin, N. Tamura, C. Tian, T.-C. Weng, X.-Q. Yang, Y. S. Meng, D. Nordlund, W. Yang, and M. M. Doeff, *Chemical Reviews* **117**, 13123 (2017).
 - [4] B. I. Cho, K. Engelhorn, A. A. Correa, T. Ogitsu, C. P. Weber, H. J. Lee, J. Feng, P. A. Ni, Y. Ping, A. J. Nelson, D. Prendergast, R. W. Lee, R. W. Falcone, and P. A. Heimann, *Phys. Rev. Lett.* **106**, 167601 (2011).
 - [5] C. Stamm, N. Pontius, T. Kachel, M. Wietstruk, and H. A. Dürr, *Phys. Rev. B* **81**, 104425 (2010).
 - [6] R. Bolis, J.-A. Hernandez, V. Recoules, M. Guarguaglini, F. Dorchies, N. Jourdain, A. Ravasio, T. Vinci, E. Brambrink, N. Ozaki, J. Bouchet, F. Remus, R. Musella, S. Mazevet, N. J. Hartley, F. Guyot, and A. Benuzzi-Mounaix, *Physics of Plasmas* **26**, 112703 (2019).
 - [7] R. M. Martin, L. Reining, and D. M. Ceperley, *Interacting electrons : theory and computational approaches* (Cambridge University Press, New York, NY, 2016).
 - [8] D. Prendergast and G. Galli, *Phys. Rev. Lett.* **96**, 215502 (2006).
 - [9] J. J. Rehr, J. J. Kas, F. D. Vila, M. P. Prange, and K. Jorissen, *Phys. Chem. Chem. Phys.* **12**, 5503 (2010).
 - [10] J. J. Kas, T. D. Blanton, and J. J. Rehr, *Phys. Rev. B* **100**, 195144 (2019).
 - [11] H. Ebert, D. Ködderitzsch, and J. Minár, *Reports on Progress in Physics* **74**, 096501 (2011).
 - [12] J. J. Kas, F. D. Vila, C. D. Pemmaraju, T. S. Tan, and J. J. Rehr, Unpublished.
 - [13] J. J. Rehr and R. C. Albers, *Phys. Rev. B* **41**, 8139 (1990).
 - [14] J. J. Kas, J. J. Rehr, and J. B. Curtis, *Phys. Rev. B* **94**, 035156 (2016).
 - [15] J. J. Rehr and R. C. Albers, *Rev. Mod. Phys.* **72**, 621 (2000).
 - [16] A. L. Ankudinov, B. Ravel, J. J. Rehr, and S. D. Conradson, *Phys. Rev. B* **58**, 7565 (1998).
 - [17] V. V. Karasiev, T. Sjoström, J. Dufty, and S. B. Trickey, *Phys. Rev. Lett.* **112**, 076403 (2014).
 - [18] J. J. Kas and J. J. Rehr, *Phys. Rev. Lett.* **119**, 176403 (2017).
 - [19] T. S. Tan, J. J. Kas, and J. J. Rehr, *Phys. Rev. B* **98**, 115125 (2018).
 - [20] U. v. Barth and L. Hedin, *Journal of Physics C: Solid State Physics* **5**, 1629 (1972).
 - [21] Z. Lin, L. V. Zhigilei, and V. Celli, *Phys. Rev. B* **77**, 075133 (2008).
 - [22] A. Mančić, A. Lévy, M. Harmand, M. Nakatsutsumi, P. Antici, P. Audebert, P. Combis, S. Fourmaux, S. Mazevet, O. Peyrusse, V. Recoules, P. Renaudin, J. Robiche, F. Dorchies, and J. Fuchs, *Phys. Rev. Lett.* **104**, 035002 (2010).
 - [23] B. I. Cho, T. Ogitsu, K. Engelhorn, A. A. Correa, Y. Ping, J. W. Lee, L. J. Bae, D. Prendergast, R. W. Falcone, and P. A. Heimann, *Scientific Reports* **6**, 18843

- (2016).
- [24] B. Mahieu, N. Jourdain, K. Ta Phuoc, F. Dorchies, J.-P. Goddet, A. Lifschitz, P. Renaudin, and L. Lecherbourg, *Nature Communications* **9**, 3276 (2018).
- [25] N. Jourdain, L. Lecherbourg, V. Recoules, P. Renaudin, and F. Dorchies, *Phys. Rev. B* **97**, 075148 (2018).
- [26] N. Jourdain, V. Recoules, L. Lecherbourg, P. Renaudin, and F. Dorchies, *Phys. Rev. B* **101**, 125127 (2020).
- [27] G. Kresse and J. Furthmüller, *Phys. Rev. B* **54**, 11169 (1996).
- [28] G. Kresse and D. Joubert, *Phys. Rev. B* **59**, 1758 (1999).
- [29] J. P. Perdew, K. Burke, and M. Ernzerhof, *Phys. Rev. Lett.* **77**, 3865 (1996).
- [30] P. Giannozzi, S. Baroni, N. Bonini, M. Calandra, R. Car, C. Cavazzoni, D. Ceresoli, G. L. Chiarotti, M. Cococcioni, I. Dabo, A. Dal Corso, S. de Gironcoli, S. Fabris, G. Fratesi, R. Gebauer, U. Gerstmann, C. Gougoussis, A. Kokalj, M. Lazzeri, L. Martin-Samos, N. Marzari, F. Mauri, R. Mazzarello, S. Paolini, A. Pasquarello, L. Paulatto, C. Sbraccia, S. Scandolo, G. Sclauzero, A. P. Seitsonen, A. Smogunov, P. Umari, and R. M. Wentzcovitch, *Journal of Physics: Condensed Matter* **21**, 395502 (19pp) (2009).
- [31] P. Giannozzi, O. Andreussi, T. Brumme, O. Bunau, M. B. Nardelli, M. Calandra, R. Car, C. Cavazzoni, D. Ceresoli, M. Cococcioni, N. Colonna, I. Carnimeo, A. D. Corso, S. de Gironcoli, P. Delugas, R. A. D. Jr, A. Ferretti, A. Floris, G. Fratesi, G. Fugallo, R. Gebauer, U. Gerstmann, F. Giustino, T. Gorni, J. Jia, M. Kawamura, H.-Y. Ko, A. Kokalj, E. Küçükbenli, M. Lazzeri, M. Marsili, N. Marzari, F. Mauri, N. L. Nguyen, H.-V. Nguyen, A. O. de-la Roza, L. Paulatto, S. Poncé, D. Rocca, R. Sabatini, B. Santra, M. Schlipf, A. P. Seitsonen, A. Smogunov, I. Timrov, T. Thonhauser, P. Umari, N. Vast, X. Wu, and S. Baroni, *Journal of Physics: Condensed Matter* **29**, 465901 (2017).
- [32] P. Giannozzi, O. Baseggio, P. Bonfà, D. Brunato, R. Car, I. Carnimeo, C. Cavazzoni, S. de Gironcoli, P. Delugas, F. Ferrari Ruffino, A. Ferretti, N. Marzari, I. Timrov, A. Urru, and S. Baroni, *The Journal of Chemical Physics* **152**, 154105 (2020).
- [33] We used the pseudopotentials Mg.pbesol-spnl-kjpaw_psl.1.0.0.UPF and O.pbesol-n-kjpaw_psl.1.0.0.UPF from <http://www.quantum-espresso.org>.
- [34] K. Nakanishi and T. Ohta, *Journal of Physics: Condensed Matter* **21**, 104214 (2009).
- [35] A. L. Ankudinov, A. I. Nesvizhskii, and J. J. Rehr, *Phys. Rev. B* **67**, 115120 (2003).
- [36] J. J. Rehr, J. A. Soininen, and E. L. Shirley, *Physica Scripta*, 207 (2005).
- [37] R. Nemausat, D. Cabaret, C. Gervais, C. Brouder, N. Trcera, A. Bordage, I. Errea, and F. Mauri, *Phys. Rev. B* **92**, 144310 (2015).